JOURNAL OF THERMOPHYSICS AND HEAT TRANSFER
Vol. 21, No. 3, July–September 2007

# Developing Consistent Inlet Boundary Conditions to Study the Entrance Zone in Microchannels

Masoud Darbandi* and Shidvash Vakilipour†
*Sharif University of Technology, 11365 Tehran, Iran*

DOI: 10.2514/1.27509

**One important point in microflow study is the correct consideration of the Knudsen layer. In addition to the many complexities behind numerical simulation of the Knudsen layer near the solid walls, there are serious uncertainties at the microchannel inlet (the point at which the flow enters the microdomain). One major difficulty is the appearance of two singularities at the two corners of the inlet section. They seriously affect the solution in the entrance region of microchannels in which the lengths are comparable with the lengths of their hydrodynamic developing zones. Although the macro inlet flow problem has been largely investigated, there has been little attempt to study the issue in microdomains. In this research, we use our experience in solving macro entry-flow problems and extend it suitably to microflow applications. To avoid the singularities and to achieve more realistic conditions at the real inlet, we implement suitable boundary conditions far upstream of the channel. This strategy reduces the erroneous role of the singularities and permits a more accurate solution in the entrance region of the microchannel. This paper deals with the numerical solution of the entrance region in short-length microchannels in which the compressibility effect is minor.**

## Nomenclature

| | | |
|---|---|---|
| $F$ | = | $x$-momentum component at node, $\rho u$ |
| $f$ | = | $x$-momentum component at integration point, $\rho u$ |
| $G$ | = | $y$-momentum component at node, $\rho v$ |
| $g$ | = | $y$-momentum component at integration point, $\rho v$ |
| $H$ | = | microchannel height |
| $Kn$ | = | Knudsen number |
| $L$ | = | microchannel length |
| $n$ | = | normal direction |
| $\tilde{P}$ | = | dimensionless pressure |
| $P$, $p$ | = | pressure at node and integration point, respectively |
| $Re$ | = | Reynolds number |
| $s$ | = | streamwise direction |
| $U$ | = | dimensionless longitudinal velocity |
| $u$, $v$ | = | longitudinal and transversal velocity components |
| $\bar{u}$ | = | mean velocity |
| $X$, $Y$ | = | dimensionless coordinates |
| $\beta$ | = | slip coefficient |
| $\lambda$ | = | mean free path of molecules |
| $\mu$ | = | fluid viscosity coefficient |
| $\rho$ | = | density |
| $\sigma$ | = | tangential momentum accommodation coefficient |
| $\tau$ | = | shear stress |

*Subscripts*

| | | |
|---|---|---|
| ip | = | integration point properties |
| $s$ | = | slip |
| $t$ | = | tangential |
| up | = | upwind |
| $w$ | = | wall |

Presented as Paper 0591 at the the 44th AIAA Aerospace Sciences Meeting and Exhibit, Reno, NV, 9–12 January 2006; received 26 August 2006; revision received 22 January 2007; accepted for publication 23 January 2007. 

*Associate Professor, Department of Aerospace Engineering, P.O. Box 11365-8639.

†Ph.D. Candidate, Department of Aerospace Engineering, P.O. Box 11365-8639.

## I. Introduction

FROM macroflow experience, the velocity distribution at the inlet of a duct undergoes a development from some initial profile at the entrance to a fully developed profile at locations far downstream. The region of duct in which this velocity development occurs is called the *entrance region*. There has been considerable interest in predicting the fluid behavior within the entrance region, because of its general technical importance in engineering applications, for example, in predicting the pressure drop in short-length conduits [1,2]. The numerical solution of the Navier–Stokes equations with no-slip boundary conditions has led to interesting conclusions for entrance flow problems. Particularly, the velocity distribution at the inlet encounters two singularities near the solid walls and results in two overshoots in the velocity profile beside the walls near the inlet region [3]. Generally speaking, the implementation of different boundary conditions at the inlet of the channels can result in different entrance-region solutions, which may be realistic or unrealistic. Wang and Longwell [4] were the first to solve the entrance flow problem, specifying zero vorticity at the inlet instead of a uniform entry condition. Mcdonald et al. [5] solved the $\psi$-$\omega$ form of the Navier–Stokes equations for the entrance region of both a tube and a channel, using either uniform or irrotational inlet boundary conditions. They concluded that irrotational entry would generate weaker singularities than uniform entry. Morihara and Cheng [6] employed the method of quasi linearization to solve for parallel plates, using uniform entry condition. They reported velocity overshoots for all Reynolds numbers; however, their magnitude decreased with increasing Reynolds number. Chen [7] employed approximate integral methods to solve for the tube and channel. He plugged a flat velocity profile in the region of the core to prohibit concavity in the midpart of the velocity profile. Chilukuri and Pletcher [8] solved partially parabolized Navier–Stokes equations for entrance flow by dropping off the viscous diffusion terms of momentum equation in the main flow direction. Abdulnour and Potter [9] reported that the overshoot would be minimal in the streamwise velocity profile near the wall if a special boundary condition treatment was applied to the $\psi$-$\omega$ form of the governing equations. Darbandi and Schneider [3] also presented a detailed investigation in the entrance region and quantified the overshoot magnitudes for a wide range of Reynolds numbers.

From a microflow perspective, the microelectromechanical systems (MEMS) are devices with a characteristic length of less than 1 mm but more than 1 $\mu$m; therefore, the flow Knudsen number in such devices is characterized between 0.01 and 0.1, which is in the

range of a slip flow regime. The correct slip-velocity boundary-condition implementation is a rather important task in simulating slip flow regime. Because of rarefaction effects, the no-slip boundary condition cannot be implemented anymore on solid boundaries [10]. For many years, the microflow through microtubes and microchannels has been largely investigated experimentally, numerically, and analytically. Contrary to macroflow investigation, the microflow literature shows that there has been less interest in evaluating the impact of the inlet boundary condition in the solution near the inlet region. Therefore, we limit ourselves to mostly inlet boundary treatment rather than the slip boundary, although the latter one is the most attractive subject in gaseous microflow treatment. Definitely, the gaseous microflow literature is very vast and we try to focus on a limited number of them, to elaborate microflow treatment and the way that the inlet boundary condition is applied at the inlet section.

Pfahler et al. [11] and Choi et al. [12] studied gaseous flow through microchannels and microtubes, respectively. They both reported a decrease in friction factor and concluded that there would be less momentum exchange between the fluid and solid surface in microchannels. Pong et al. [13] measured the pressure distribution in microchannels and concluded that the distribution would not be a linear function of its streamwise distance. Beskok and Karniadakis [14] used a computational tool, modeled the slip flow regime in a microchannel, and verified the observations on friction reduction reported by [11,12]. The 2-D computations closely matched the friction factors of Pfahler et al.; however, the analysis did not provide a clear Reynolds dependence on friction factor. Shih et al. [15] performed an experiment using a microchannel with $L/H = 4000/1.2$ to measure the mass flow rate and the axial pressure distribution along a microchannel for helium and nitrogen. They compared the results of their experiment with those of compressible analytical solution derived under isothermal conditions. The results with helium were in reasonable agreement with the slip flow prediction. Arkilic et al. [16] also carefully studied and analyzed compressible rarefied gas flow in long 2-D microchannels (e.g., $L/H = 7500/1.33$). They even used the Navier–Stokes equations for small Knudsen numbers and compared their theoretical outcomes with the experiments of Pong et al. [13]. They concluded that their analytical solution, which took into account both the compressibility and rarefaction effects via implementing the slip flow boundary condition, would agree favorably with the measurement. However, the incompressible solution predicted a linear pressure drop in the same inlet-to-outlet pressure ratio, indicating that there would be deviation from the experiment. They confirmed that the density would decrease and thus the velocity would increase in the streamwise direction in compressible flow through a constant-area duct. As a result, the pressure distribution would be nonlinear with negative curvature. A moderate Knudsen number (a moderate slip) would actually diminish, albeit rather weakly, this curvature. Thus, the compressibility and rarefaction effects led to opposing trends.

Kavehpour and Faghri [17] adopted a control volume method to solve the 2-D fluid flow governing equations in a long microchannel with $L/H = 8000$ and to study the rarefaction effects. They compared their computations with the experiments performed by [11,15,16] and showed that there would be very good agreement with theirs. Moreover, they studied normalized friction coefficient and Nusselt number variations with the Reynolds and Knudsen numbers and showed that the increase in the Knudsen number would cause a decrease in friction coefficient and Nusselt number, because of rarefaction effects. They specified a uniform axial velocity and a zero transverse velocity at the inlet section. Their velocity profiles showed overshoots near the inlet section. Guo and Wu [18] also carried out a numerical study on the compressibility effect of gas flow in a microtube and indicated that the dimensionless velocity profile and friction factor were functions only of the local Mach number, if the entrance effect could be neglected. They applied a fully developed no-slip profile at the inlet of the microtube. Therefore, the calculation in the entrance region would be uncertain. Beskok and Karniadakis [19] investigated rarefied gas flow and developed a simple physical-based model to predict mass flow rate. For the channel, the length-to-height ratio and inlet-to-outlet pressure ratio were 20 and 2.28, respectively. In their study, the velocities were obtained using Navier–Stokes equations subject to second-order slip boundary conditions. Similar to [18], Barber and Emerson [20] applied a no-slip fully developed velocity profile at the microchannel inlet. Although the solution in the transition region cannot be realistic, the achieved fully developed slip velocity profile can be acceptable, providing that the slip flow regime remains in the incompressible limit. Karniadakis and Beskok [10] applied uniform axial velocity and zero transverse velocity as the inlet flow condition in their $\mu$-flow code. They used high-order elements and discussed the overshoots appearing at those sections.

Ahmed and Beskok [21] investigated the simulation of gaseous microflow through microfilters for continuum and slip flow regimes via solving the spectral element formulations of compressible Navier–Stokes equations. They showed that the compressibility effect would become important for high-speed flows, which created large density fluctuations across the microfilter element. They specified the inflow and outflow boundary conditions sufficiently away from the flow domain; however, they did not explicitly indicate which type of boundary conditions they employed at those far boundaries. Their inlet boundary condition is likely very similar to the one used in this work; however, they did not focus on the details of developing zones in a microchannel, but reported the solution at the mid cross section of a convergent-constant-divergent channel, irrespective of the flow condition there. Choi et al. [22] proposed a new slip model called the *Langmuir slip condition* to analyze the steady isothermal gaseous microflow in a microchannel with $L/H = 30/1.12$, using the numerical modeling of the Navier–Stokes equations. They applied a slip condition close to the Maxwell slip condition at the inlet section. Their results showed that the pressure nonlinearity would decrease close to the inlet section. Asako and Toriyama [23] used the isentropic relations between the stagnation condition, located far upstream of the inlet section, and the inlet section and calculated a uniform longitudinal velocity with zero transverse component at the inlet section. Raju and Roy [24] used a finite element hydrodynamic model to simulate subsonic gaseous flow through very long microchannels. They applied $\partial u/\partial x = v = 0$ at the inlet and specified pressure at the outlet. Their results showed that the nonlinearity effect would be negligible close to the inlet. Alternatively, Raju and Roy [25] used the same model to simulate supersonic gaseous flow through microchannels. They neglected the end effects in their numerical simulation. Similar to supersonic macroflow considerations [26,27], they fixed all flow variables such as velocity, temperature, and density at the inlet section. They also used uniform axial and zero transversal velocities at the inlet. Renksizbulut et al. [28] applied inflow boundary conditions corresponding to uniform flat profiles. The so-called velocity overshoots can be clearly observed in their velocity profiles.

The entrance flow problem is similarly encountered in methods that take into account the motions and collisions of the molecules within the computation domain [29]. For example, Shen et al. [30] used information preservation and direct simulation of Monte Carlo (DSMC) methods and studied the rarefaction effects in long and short microchannels. Contrary to the long microchannel cases, the rarefaction effects become weak in short microchannels. Their channel dimension was $L/H = 15$. They defined their microchannel and its boundary conditions in a manner that made DSMC calculations affordable. They compared the results of their two methods with that of the Navier–Stokes solution, employing a velocity-slip boundary condition. They showed that the three results agreed well with each other without exhibiting strong nonlinearity effect in pressure distribution. Shu et al. [31] and Niu et al. [32] proposed a lattice Boltzmann BGK model to simulate the developing microflow in 2-D microchannels with $L/H = 20$ for low Reynolds and Knudsen numbers flows. They imposed uniform velocity at the inlet of the channel and extrapolated the variables at the outlet from the interior flowfield. Moreover, Le and Hassan [33] used the DSMC method and applied a freestream boundary condition at the inlet of their microchannels. However, to ensure the freestream condition

there, a portion of the wall at the entrance region (say, 10%) of the entire channel was taken as a specular reflector.

The previous literature shows that there has been less interest in studying the details of the solution in the entrance region of the microchannels, mainly because the chosen microchannels have mostly been very long, resulting in negligible entrance length compared with the entire length of the channel. Contrary to long microchannels, the short ones need special care and caution, because the entrance region occupies a significant, if not the entire, part of the computational domain. As raised by Arkilic et al. [16], the existence of nonzero wall velocity also affects the flow profiles that are present in the entrance region of the channel. A primary feature of slip flow within the developing region of the channel is the possible existence of off-centerline maximum streamwise velocities [34]. This phenomenon can remarkably affect the dynamics of short channels and is important for related applications, which are briefly described in the next section. In the authors' opinion, the issue of inlet flow condition has not been fully resolved in macrochannels yet, because different boundary conditions may result in different entrance-region solutions [2–9]. This issue must be more serious and even worse in microchannels, because the boundary conditions at the outlet of the microchannels are more ambiguous than those in macrochannels. For example, achieving a fully developed no-slip profile at the outlet section of a long macrochannel is quite reasonable; however, the velocity profile at the outlet of a microchannel is not known before the solution. In the current work, we show that the inlet boundary condition has important impact in numerical simulation of the microflow in short microchannels. To improve the solution, we use our experience in macro entry-flow treatment [2,3] and present suitable boundary conditions at the inlet section of the microchannels that reduce the erroneous impact of the two singularities appearing at the inlet of the microchannels. This consideration is achieved via implementing the inlet boundary condition at a station located far upstream of the real inlet section [35]. This strategy results in a more realistic boundary condition at the real inlet of short microchannels; additionally, it results in a more realistic solution for the entrance region.

## II. Slip Boundary Analysis

As indicated by Barber and Emerson [20], one major difficulty in predicting gaseous transport in microchannels can be attributed to the fact that the continuum flow assumption considered in establishing the Navier–Stokes equations is no longer valid when the mean free path of the molecules is comparable to the characteristic dimensions of the channel. Under these conditions, the momentum transfer starts influencing the discrete molecular composition of the gas, and a variety of noncontinuum or rarefaction effects are likely to be exhibited. Velocity profiles, volume rates of flow, and wall shear stresses are all affected by the noncontinuum influence. For example, it is well known that the viscosity in the Knudsen layer is lower in comparison with the viscosity in the bulk fluid, as a result of the interaction of the molecules with a wall. The Maxwell slip condition depends on the normal gradient of the tangential velocity on the wall. The reduction of the viscosity increases the tangential velocity and decreases its normal gradient, therefore, it increases the slip [36]. The kinetic theory of gases relates the tangential velocity slip at the wall to the local shear through a series expansion in the mean free path or, equivalently, in the Knudsen number [37].

In this section, we present a theoretical procedure to analyze the flow inside a 2-D microchannel with noncontinuum effects near its wall. This geometry forms the limiting flow condition for rectangular ducts with a large aspect ratio, commonly encountered in microfluidic devices (e.g., shear stress tensors and microaccelerometers). We assume that the pressure loss is low enough to achieve a fully developed condition in the channel and does not vary along the rest of channel. It is known that the compressibility effects can be assumed to be dominant if there are large (say, more than 10%) density variations in the channel. This normally happens if a significant pressure ratio is applied along the channel. Indeed, low-pressure drops negligibly affect the density variation in a channel [38]. Considering this point, we assume that the gaseous microflow is almost incompressible in our analysis. This situation is mostly encountered in microchannels with short lengths; however, the length would be long enough to permit a fully developed condition at the channel exit. If the channel is sufficiently short, the Knudsen number, pressure drop, density, etc., can be assumed to be constant along the microchannel. This has a few applications in microdevices such as the free molecular microresistojet, which operates on the principle of electrothermal propulsion [39,40]. On the other hand, the advancement in microfabrication technology has enabled the possibility of developing thin filters with sufficient strength to provide desirable flow rates in suitable pressure differences. The microflow can be viewed as a short-length microchannel or sudden constriction in the flowfield; therefore, simple analysis based on the fully developed flow assumption cannot be valid for them [41]. Another application can be a microblowing system, in which a secondary microflow is injected into the main flow through microholes (or short-length microchannels) fabricated in the microplate subject to the main flow [42].

The velocity profile for incompressible laminar flow can be readily obtained from the simplified form of the axial momentum equation. In this section, we follow the analytical procedure presented by Barber and Emerson [20]. They examined the effects of Reynolds and Knudsen numbers on the hydrodynamic development lengths in circular and parallel plate ducts. However, contrary to the reference, we derive our expressions based on the channel height instead of its hydraulic diameter. Assuming a fully developed flow through our 2-D microchannel, the velocity component in the transverse direction vanishes, and the velocity component in the longitudinal direction will become a function of $y$ only. The analysis of the $y$-momentum equation results in a constant pressure at each cross section. Considering the preceding theories, the flow can be completely described by the axial momentum equation, which is given by

$$\mu \frac{d^2u}{\mathrm{d}y^2} = \frac{\mathrm{d}p}{\mathrm{d}x} \tag{1}$$

where $\mathrm{d}p/\mathrm{d}x$ presents the axial pressure drop. To apply the noncontinuum flow effects in the vicinity of the wall, Eq. (1) can be solved using the slip velocity boundary condition proposed by Basset [43]. For the nonstationary walls, the slip condition can be related to the tangential shear stresses and the wall velocity via

$$\tau_t = \beta(u_s - u_w) \tag{2}$$

Schaaf and Chambre [44] showed that the slip coefficient can be related to the mean free path of the molecules by

$$\beta = \mu/\{[(2-\sigma)/\sigma]\lambda\} \tag{3}$$

The shear stress on the lower and upper walls of the channel (i.e., $y = 0$ and $H$) can be related to the velocity gradient. For the lower wall, it yields

$$\tau_t = \mu \left.\frac{\mathrm{d}u_s}{\mathrm{d}n}\right|_{y=0} \tag{4}$$

In this work, $H$ is chosen as the characteristic length scale to define both the Reynolds and Knudsen numbers, which are defined as

$$Re = \rho\bar{u}H/\mu \qquad Kn = \lambda/H \tag{5}$$

where the mean velocity is calculated from

$$\bar{u} = \frac{1}{H}\int_0^H u(y)\,\mathrm{d}y \tag{6}$$

To present our derived expressions in dimensionless form, the velocity, pressure, length, and height of the microchannel are nondimensionalized by

$$U = u/\bar{u}, \qquad \tilde{P} = p/\rho\bar{u}^2, \qquad X = x/H, \qquad Y = y/H \tag{7}$$

Substituting Eqs. (3) and (4) into Eq. (2) and using the Knudsen number definition, the nondimensional tangential slip velocity at the bottom wall is derived as

$$U_s - U_w = \frac{2-\sigma}{\sigma} Kn \left.\frac{\mathrm{d}U_s}{\mathrm{d}n}\right|_{y=0} \tag{8}$$

Considering Eq. (1) as a linear second-order ordinary differential equation, the longitudinal velocity profile has a second-order polynomial form, given by $u(y) = a_2 y^2 + a_1 y + a_0$. The constants $a_0$, $a_1$, and $a_2$ can be easily obtained for a symmetric velocity-profile condition at the channel centerline and two slip boundary conditions at its corresponding walls. Applying these conditions, the nondimensional velocity profile across the microchannel is derived as follows:

$$U(Y) = -\frac{Re}{2}\frac{\mathrm{d}\tilde{P}}{\mathrm{d}X}\left(Y - Y^2 + \frac{2-\sigma}{\sigma} Kn\right) \tag{9}$$

Obviously, in the limit of $Kn \to 0$, Eq. (9) reduces to the familiar no-slip velocity profile for parallel flow through a macrochannel. Substituting Eq. (9) into Eq. (6) and integrating it eventually leads to the mean dimensionless slip velocity profile, as follows:

$$\bar{U} = -\frac{Re}{12}\frac{\mathrm{d}\tilde{P}}{\mathrm{d}X}\left(1 + 6\frac{2-\sigma}{\sigma} Kn\right) \tag{10}$$

This is similarly reported by Shih et al. [15]. Equations (9) and (10) can be assembled to give the velocity profile across the microchannel in term of the mean velocity, which yields

$$U(Y) = 6\bar{U}\left(Y - Y^2 + \frac{2-\sigma}{\sigma} Kn\right) \Big/ \left(1 + 6\frac{2-\sigma}{\sigma} Kn\right) \tag{11}$$

This profile indicates that for a fixed mean velocity, the fully developed slip velocity profile is independent of the Reynolds number and pressure drop along the channel. If the inlet velocity profile far upstream of the channel (i.e., $x = -\infty$) has a uniform distribution with $u_{\text{in}} = 1$, the average velocity should be equal to unity at any arbitrary cross section along the microchannel. Equation (11) is then reduced to

$$U(Y) = 6\left(Y - Y^2 + \frac{2-\sigma}{\sigma} Kn\right) \Big/ \left(1 + 6\frac{2-\sigma}{\sigma} Kn\right) \tag{12}$$

Assuming an incompressible flow, Eq. (10) can be inversely used to calculate dimensionless pressure drop along the channel, which yields

$$\frac{\mathrm{d}\tilde{P}}{\mathrm{d}X} = -12\bar{U}\left[Re\left(1 + 6\frac{2-\sigma}{\sigma} Kn\right)\right]^{-1} \tag{13}$$

Once more, it is essential to reemphasize that the current derivations are valid if the microchannel length is sufficiently short. In the Results section, we show that the compressibility effect becomes negligible along the channel in such conditions. Hence, the preceding derivations are only valid to verify the results in short microchannels with minor compressibility effect.

## III. Governing Equations

The steady-state form of the conservation laws for mass and momentums are given by

$$\frac{\partial \boldsymbol{F}(\boldsymbol{\psi})}{\partial x} + \frac{\partial \boldsymbol{G}(\boldsymbol{\psi})}{\partial y} = \frac{\partial \boldsymbol{R}(\boldsymbol{\psi})}{\partial x} + \frac{\partial \boldsymbol{T}(\boldsymbol{\psi})}{\partial y} \tag{14}$$

where the solution vector $\boldsymbol{\psi}$, convection vectors $\boldsymbol{F}$ and $\boldsymbol{G}$, and diffusion vectors $\boldsymbol{R}$ and $\boldsymbol{T}$ are defined as

$$[\boldsymbol{\psi}\ \boldsymbol{F}\ \boldsymbol{G}\ \boldsymbol{R}\ \boldsymbol{T}] = \begin{bmatrix} \rho & \rho u & \rho v & 0 & 0 \\ \rho u & \rho uu + p & \rho vu & \tau_{xx} & \tau_{yx} \\ \rho v & \rho uv & \rho vv + p & \tau_{xy} & \tau_{yy} \end{bmatrix} \tag{15}$$

The continuity, $x$-momentum, and $y$-momentum equations are represented by the first, second, and third lines, respectively, in Eq. (15). For a low-speed flow with isothermal conditions, the energy equation is not involved in the system of governing equations. The Newtonian fluid assumption is used to present the stress terms, which yields

$$\tau_{xx} = 2\mu\frac{\partial u}{\partial x} - \frac{2}{3}\mu\left(\frac{\partial u}{\partial x} + \frac{\partial v}{\partial y}\right) \qquad \tau_{yy} = 2\mu\frac{\partial v}{\partial y} - \frac{2}{3}\mu\left(\frac{\partial u}{\partial x} + \frac{\partial v}{\partial y}\right) \tag{16a}$$

$$\tau_{xy} = \tau_{yx} = \mu\left(\frac{\partial u}{\partial y} + \frac{\partial v}{\partial x}\right) \tag{16b}$$

Because the flow is assumed to be compressible, the equation of state $P = \rho RT$ for ideal gases is used to relate the density and pressure fields to the constant temperature field.

## IV. Numerical Modeling

Assuming a simple rectangular solution domain, we apply the structured triangular grid to discretize it. However, our original numerical tool is also capable of treating flow on unstructured grids [45]. Figure 1 shows part of an unstructured grid. In a finite element approach, nodes are located at three corners of each element (see the solid circles in Fig. 1). Each element is broken into three subcontrol volumes (SCVs) using the three medians of each triangle (see element PMS). The proper assemblage of the discrete subcontrol volumes from different neighboring elements creates a closed area around each node, which can be subsequently used to employ the conservation laws (see the shaded area in Fig. 1). As shown, there are three cell faces in each element. The fluxes on each of these three faces are estimated at their midpoints, which are called the *integration points* (see $ip_1$ and $ip_2$ in the PSR element). Normal direction to each cell face is needed for integrating purposes. The normal vectors are directed outward to the faces of each SCV. For $\text{SCV}_i$ in element PTN, only the fluxes pass through the inner surfaces of $\text{SCV}_i$ (i.e., S1$i$ and S2$i$) need to be considered in conservation treatment. Therefore, we only need to calculate the fluxes at the integration point of the inner faces. However, the unknowns at the integration points are not the major unknowns and must be presented in terms of nodal unknowns, to close the resulting system of algebraic equations properly.

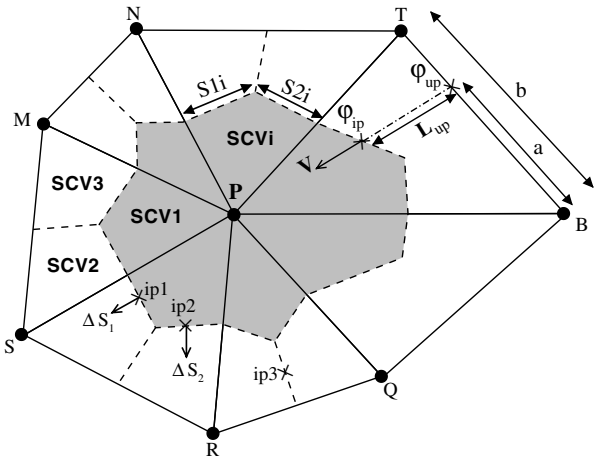


**Fig. 1 Finite volume element grid and the schematic of upwind strategy within the elements.**

The Navier–Stokes equations without any source term consist of two major convection and diffusion parts. A numerical approach is successful if it uses correct physics to model these two parts. The present numerical approach is a finite volume method, but it benefits from the specific advantages of the finite element method. We intend to use the correct physics of each term in its discretization. In this regard, the gradients of finite element shape functions are used to treat the pressure and diffusion terms, which resemble an elliptic nature. However, the convection part is more complex and its discretization needs careful attention.

The present method is pressure-based and considers this variable as an unknown in its algorithm. In many pressured-based algorithms, the velocity components (i.e., $u$ and $v$) are chosen as the major unknowns. In the present research, the momentum components [i.e., $F(=\rho u)$ and $G(=\rho v)$] are chosen as the major unknowns. Because this study is at the beginning of a general research that intends to develop an all-speed algorithm for microflow analysis, we chose our dependent variables in a manner that permits extending our current formulations to solve flow at all speeds, with minimum difficulties [26,27,46].

Considering the preceding points and using the advantages of divergence theorem, Eq. (14) is integrated over an arbitrary SCV (see the shaded SCV in element PTN in Fig. 1), which yields

$$\int_{S1i} (\boldsymbol{F}\hat{i} + \boldsymbol{G}\hat{j}) \cdot \boldsymbol{ds} + \int_{S2i} (\boldsymbol{F}\hat{i} + \boldsymbol{G}\hat{j}) \cdot \boldsymbol{ds} = \int_{S1i} (\boldsymbol{R}\hat{i} + \boldsymbol{T}\hat{j}) \cdot \boldsymbol{ds} + \int_{S2i} (\boldsymbol{R}\hat{i} + \boldsymbol{T}\hat{j}) \cdot \boldsymbol{ds} \tag{17}$$

where $S1i$ and $S2i$ are the two main cell faces in that SCV. The substitutions of $\boldsymbol{F}$, $\boldsymbol{G}$, $\boldsymbol{R}$, and $\boldsymbol{T}$ vectors from Eq. (15) into Eq. (17) produce three conservation statements for mass and momentums. In the present approach, the fluxes at the SCV faces are assumed to be uniform. The total flux magnitude is placed at the integration points (see the × symbols in Fig. 1). For example, the calculation of mass fluxes at the integration points and their substitution in the continuity equation finally result in [45]

$$[a^{pfm}]\{f\} + [a^{pgm}]\{g\} = 0 \tag{18}$$

Equation (18) is in matrix form and presents three mass conservations within three SCVs in each element. In other words, this equation includes three equations for three SCVs in each element. The vectors shown by the lowercase letters $f$ and $g$ represent quantities at integration points, which should be properly presented in terms of nodal quantities. The superscripts over the matrix elements annotate the names of the equation (e.g., $p$ for the continuity equation), the corresponding unknown variable (e.g., $f$ for the unknown $f$ variable), and the essence of term ($m$ for the mass flux, $d$ for the diffusion, $p$ for the pressure, and $c$ for the convection terms) from left to right, respectively. Back to the first line in Eq. (15), the elements of the matrix in Eq. (18) can be calculated from

$$a_{i,j}^{pfm} = \begin{cases} (\Delta S_x)_{S1i} & j = S1i \\ (\Delta S_x)_{S2i} & j = S2i \\ 0 & \text{else} \end{cases} \qquad a_{i,j}^{pgm} = \begin{cases} (\Delta S_y)_{S1i} & j = S1i \\ (\Delta S_y)_{S2i} & j = S2i \\ 0 & \text{else} \end{cases} \tag{19}$$

where the index $i$ is the SCV number and index $j$ is the integration point number, and $\Delta S_x$ and $\Delta S_y$ are the length of the normal vector component in the $x$ and $y$ directions, respectively. The momentum equations in the $x$ and $y$ directions can be treated in a similar manner. Their closed forms can be eventually written as [45]

$$[A^{ffd}]\{F\} + [A^{fgd}]\{G\} + [a^{ffc}]\{f\} + [a^{fpp}]\{p\} = \{A^{fd}\} \tag{20a}$$

$$[A^{gfd}]\{F\} + [A^{ggd}]\{G\} + [a^{ggc}]\{g\} + [a^{gpp}]\{p\} = \{A^{gd}\} \tag{20b}$$

In the preceding equations, the upper case $F$ and $G$ represent the nodal magnitudes (i.e., the magnitudes at the solid circles in Fig. 1).

Because $f$, $g$, and $p$ in Eqs. (18) and (20) are computed at integration points, it is necessary to develop suitable relations between integration and nodal points to construct a well-posed set of linear algebraic equations. In other words, $f$, $g$, and $p$ must be suitably expressed in terms of $F$, $G$, and $P$. In this regard, the pressure is approximated using the finite element shape functions, that is,

$$p_i = \sum_{j=1}^{3} N_j P_{ij}$$

However, the convection terms play more complex physics. Therefore, we focus on these terms, which mainly affect the accuracy of the solution. The velocity components in the Navier–Stokes equations are categorized into convected and convecting types, which provide the required coupling between the velocity and pressure fields in our collocated grid approach [47,48]. All of the velocities in the continuity equation are the convected type, but the velocities in the momentum equations can be regarded as both types. The convecting velocities transport a property in the solution domain; hence, the upwind physics is a suitable option to approximate them. It is known that the primitive upwind-based methods are prone to produce false diffusion. For the streamwise upwind strategy, a suitable magnitude of a scalar $\varphi$ at an integration point can be estimated from

$$\varphi_{\text{ip}} = \varphi_{\text{up}} + \Delta\varphi_{\text{ip}} \tag{21}$$

where $\Delta\varphi_{\text{ip}}$ represents the variation of $\varphi_{\text{ip}}$ in the streamwise direction. To provide an inclusive approximation for it, the momentum equations are written in the streamwise direction, which yields [45,49]

$$V_{\text{tot}} \frac{\partial f}{\partial s} - \mu \nabla^2 u = -\frac{\partial p}{\partial x} \tag{22a}$$

$$V_{\text{tot}} \frac{\partial g}{\partial s} - \mu \nabla^2 v = -\frac{\partial p}{\partial y} \tag{22b}$$

where $V_{\text{tot}} = (u^2 + v^2)^{1/2}$. These two equations are used to approximate $f$ and $g$ in Eq. (20). For element PBT in Fig. 1, the upwind point $\varphi_{\text{up}}$ is located at the upwind edge, at the point at which the streamwise vector intersects it. The length of the line between the integration point and its upwind point is called the *upwind length* and is shown by $L_{\text{up}}$. By this definition, the gradient of $f$ along the streamwise direction can be approximated from

$$\left(V_{\text{tot}} \frac{\partial f}{\partial s}\right)_{\text{ip}i} \approx \left(V_{\text{tot}} \frac{f - f_{\text{up}}}{L_{\text{up}}}\right)_{\text{ip}i} \tag{23}$$

where $f_{\text{up}}$ can be calculated from $(f_{\text{up}})_{\text{ip}i} = (a/b)(F_{\text{upr}})_{\text{ip}i} + (1 - a/b)(F_{\text{upl}})_{\text{ip}i}$, where upr and upl denote the right and left nodes to the upwind point (see Fig. 1). The suitable treatments and rearrangements of Eqs. (22a) and (22b) finally produce two basic expressions for $f$ and $g$ at cell faces that are given by [45]

$$\{f\} = [C^{ff}]\{f\} + [C^{fp}]\{P\} + \{C^f\} \tag{24a}$$

$$\{g\} = [C^{gg}]\{G\} + [C^{gp}]\{P\} + \{C^g\} \tag{24b}$$

where $C^{**}$ and $C^{*}$ represent $3 \times 3$ matrices of coefficients and $3 \times 1$ arrays of coefficients, respectively. The current superscripts have the same definitions provided for the corresponding superscripts given on Eq. (18). If Eqs. (24a) and (24b) are substituted in both Eqs. (18) and (20), the velocity-pressure decoupling problem is not resolved completely. Rhie and Chow [47] suggested the use of two types of velocity components at the cell faces to overcome the problem. However, Darbandi and Bostandoost [48] presented a range of momentum components in their algorithm using the proper assemblages of the continuity and momentum equations. Using the latter idea, two new statements for the cell-face momentum

components are eventually obtained using suitable incorporations of the mass and momentum equations. They are shown by $\hat{f}$ and $\hat{g}$ and are written as [45]

$$\{\hat{f}\} = [C^{\hat{f}f}]\{F\} + [C^{\hat{f}g}]\{G\} + [C^{\hat{f}p}]\{P\} + \{C^{\hat{f}}\} \tag{25a}$$

$$\{\hat{g}\} = [C^{\hat{g}f}]\{F\} + [C^{\hat{g}g}]\{G\} + [C^{\hat{g}p}]\{P\} + \{C^{\hat{g}}\} \tag{25b}$$

These statements are used to approximate $f$ and $g$ in Eq. (18). The superscripts are defined as before, except annotating the first characters with a hat (i.e., $C^{\hat{**}}$ and $C^{\hat{*}}$) to distinguish them from the preceding cases. This substitution ends the numerical treatment of the governing equations. However, the next step is to assemble the constructed element stiffness matrices into the global matrix and solve them for $F$, $G$, and $P$. Because our concern in this research is not with the Navier–Stokes solver, we leave the rest to the interested readers to pursue the details in [45,46,48–50].

## V. Boundary Conditions and Grid Distribution

For a low Reynolds number of unity, our short microchannel is chosen long enough ($L/H = 2$) to achieve a fully developed status at its exit. However, it is worth mentioning that the current authors have already shown that their basic Navier–Stokes solver would be robust enough to solve long macrochannels precisely, despite applying the outlet boundary conditions at the improper locations very close to the inlet section, in which the flow is not certainly developed [51]. To reduce unnecessary computational cost, the flow is solved only for the upper half of the microchannel benefiting from the symmetric boundary conditions employed at the channel centerline. The channel length is discretized to 70 divisions, using a non-uniform hyperbolic distribution. In other words, a unit length is broken into $N$ divisions, in which the lengths vary from $\delta h_1$ to $\delta h_2$. The latter grid spacing constants are defined as [52]

$$A = \sqrt{\delta h_2}/\sqrt{\delta h_1} \qquad B = (N\sqrt{\delta h_1 \cdot \delta h_2})^{-1} \tag{26}$$

Using $B$ as a space control parameter, the distribution factor $\delta$ is determined by solving the sine hyperbolic equation, given by

$$\sinh(\delta)/\delta = B \tag{27}$$

Eventually, the distributions are obtained from

$$S(i) = \frac{w(i)}{A + (1 - A)w(i)} \tag{28}$$

where

$$w(i) = \frac{1}{2}\left\{1 + \frac{\tan[\delta(i/N - 1/2)]}{\tanh(\delta/2)}\right\}$$

In the transverse direction, one half of the channel height is uniformly discretized to 20 divisions. The slip velocity boundary condition is implemented at the solid wall using the first-order Maxwell relation [i.e., Eq. (8)], which is upgraded to

$$U_s - U_w = \frac{2 - \sigma}{\sigma} Kn \left(\frac{\partial U_s}{\partial n}\right)^{\text{old}} \tag{29}$$

In the limit of $Kn = 0$, Eq. (29) reduces to $U_s = U_w$, which is the familiar no-slip boundary condition.

As mentioned in the Introduction, there have been major problems with the types of boundary condition to be implemented at the inlet of the macrochannels [2–9]. Experimentally, it is very difficult to set the uniform or irrotational entry conditions at the inlet of conduits. Burke and Berman [53] attempted to measure the velocity profile in the entrance zone of pipes. They reported overshoots in the velocity profile close to the inlet. Other numerical researchers also confirmed the nonuniformity in the velocity profiles close to the entrance section. Darbandi and Schneider [3] studied these overshoots numerically to obtain the Reynolds number and grid resolution effects on the magnitudes and behaviors of overshoots close to macrochannel inlets. Furthermore, previous investigators reported that the use of coarse-grid resolution would not generally result in observing the overshoot, because the overshoots would be generated very close to the inlet section and near the walls. From the microchannel perspective, these overshoots would cause difficulties in applying a slip velocity condition on the walls near the inlet, because there is an abrupt jump from a unit velocity magnitude on the node located at the intersection of the inlet section and the solid wall to a nonunit magnitude on its neighboring node. To overcome the problem, Barber and Emerson [20] applied a no-slip parabolic velocity profile at the inlet section of the microchannel. This type of boundary condition is less problematic, because a zero velocity magnitude at the corner point gradually increases and reaches suitable slip velocity magnitude on its downstream neighboring nodes located on the solid wall. In other words, no abrupt jump is enforced at the inlet section. Evidently, this type of inlet boundary condition does not result in accurate solution in the entrance region. On the other hand, the use of other types of inlet velocity profiles at the inlet would cause different magnitudes of overshoot in the velocity profiles appearing in the entrance region. Our experience shows that the sensitivity to slip boundary conditions can still be troublesome near the inlet (specifically, at high Knudsen numbers), despite introducing and using different inlet boundary conditions. To avoid this numerical singularity, we extend the channel to its upstream region fictitiously. Figure 2 shows the geometry and boundary conditions used to treat microflow in the extended microchannel domain. As shown, assuming a fully developed condition at the outlet section, we specify a uniform pressure distribution $P = P_{\text{out}}$ at the outlet. However, we carefully check this assumption in the Results section. The symmetric boundary conditions are forced at the centerline.

For the extended channel shown in Fig. 2, the inlet boundary conditions are implemented at the fictitious inlet located at $x/H = -2$. The implemented boundary conditions are freestream conditions. In other words, a constant velocity profile with $u = 1.0$ and $v = 0$ is implemented at the fictitious section. As mentioned before, the symmetric boundary conditions are properly applied on the extended channel wall, to transport the freestream condition suitably from the fictitious section to the actual inlet. We distribute 30 nodes before the channel entrance. In other words, the primitive grid distribution is increased from $40 \times 20$ to $70 \times 20$, to maintain the same grid resolution in our extended computational domain. Figure 3 shows the chosen computational domain. As observed, the grid was suitably clustered close to the singular point from both the left and right sides, using the functions given in Eqs. (26–28). Indeed, the grid clustering is required at the inlet to achieve a suitable grid-independent solution near the wall [3].

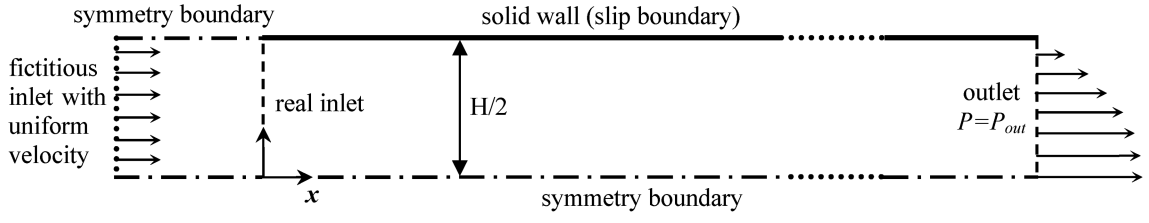


**Fig. 2 Geometry and boundary conditions to treat the microchannel.**

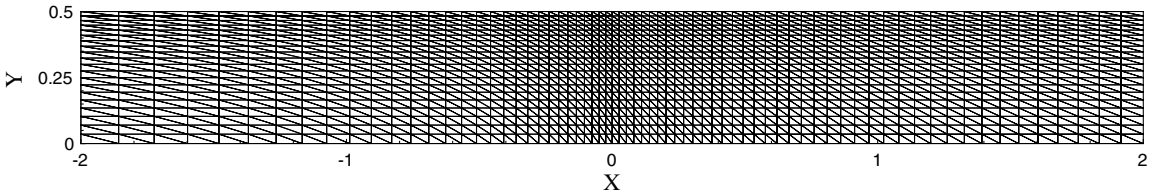


**Fig. 3 Grid in the chosen computational domain.**

Following Guo and Wo [18] and Barber and Emerson [20], we also examine their inlet boundary conditions, which are implemented at the real inlet section of the channel. In this regard, a fully developed inlet velocity profile with $u = 6(y - y^2)$ and $v = 0$ is implemented at $x/H = 0$. In all of our microflow test cases, we use the no-slip flow solution as our initial condition. The final solution is obtained via iterations on Eq. (29). In other words, after obtaining the velocity field at the end of one iteration, the gradient term in Eq. (29) is calculated using the magnitudes from the converged solution at the preceding iteration. The slip velocities on the channel wall are then updated in the next iteration. These steps are repeated until converging to an invariant slip velocity at the solid wall.

## VI. Results

Back to Fig. 2 and Eq. (5), the Reynolds number is $Re = 1$. At the beginning, we would like to verify our results against other trustworthy solutions. As described in the Introduction, the microchannel literature shows that there has been less interest in studying microchannels with short lengths. To validate our developed algorithm and the extended formulation, we ignore the computational domain introduced in the preceding section and define our channel long enough to be able to compare our result with other reliable solutions available in literature. To compare our results with the analytical solution provided by Arkilic et al. [16], the channel dimension is chosen as $L/H = 40$. Following the idea presented in Fig. 2, the dimension of computational domain is $-2 \leq x/H \leq +40$. We present our results for $Kn = 0.0$, 0.1, and 0.165, which are defined based on the flow condition at the channel outlet. Figure 4 shows the pressure distribution along the channel. The three distributions indicate that the pressure drop is close to linear in higher Knudsen numbers (or the transition regime) and becomes nonlinear in the slip flow regime. As expected, the pressure drop increases as the Knudsen number decreases. Additionally, the rate of pressure drop increases along the channel, irrespective of the Knudsen number. The current results agree well with those of the reference, even in the transition regime with $Kn = 0.165$.

In short microchannel cases, we verify our numerical solutions against either the analytical solution of Arkilic et al. [16] or the analytical solution described in Sec. III, as applicable. We present our results using a reference Knudsen number based on the condition at the channel inlet, which is almost invariable along the chosen microchannel, because of its short length. The inlet Mach number is 0.01, and its variation along the channel is less than 0.4%. Figure 4 shows that the pressure distribution is almost linear close to the inlet section of long channels, irrespective of the employed Knudsen number. Indeed, the nonlinearity is more pronounced in the region far from the inlet section. Therefore, we would expect an almost linear pressure drop in our short microchannel. Jang and Wereley [54] presented analytical derivation and experimental data for the slip flow regime in straight microchannels. They conducted their research on the location of the maximum deviation from the linear pressure distribution. They reported that the location of the maximum deviation would increase with increasing pressure ratio. Figure 5 shows our numerical pressure drop computations (symbols) and compares them with the current analytical solutions and the analytical solutions given by Arkilic et al. [16]. The comparisons are provided for a few Knudsen numbers and are limited to the real zone of the channel, for which the analytical solutions seem applicable. The figure indicates that there is good agreement among the three solutions. The nonlinearity of the numerical solution close to the inlet section is because of the developing zone, which is described shortly. Both analytical solutions do not predict this nonlinearity. As shown, the pressure drop is less than 0.4% along the entire channel, indicating that the nonlinearities of Knudsen, Mach, etc., are unimportant in such short channels. Therefore, we trust our analytical solution and verify our results against them when it seems necessary or informative.

Figure 6 shows the pressure drop along the short microchannel for a few Knudsen numbers. Figure 6a presents the pressure distribution on the channel centerline, and Fig. 6b demonstrates it along the upper boundary of the computational domain. The figures show that there are nonlinear pressure drops in the region close to the real inlet section. However, the pressure drops are linear before and after this

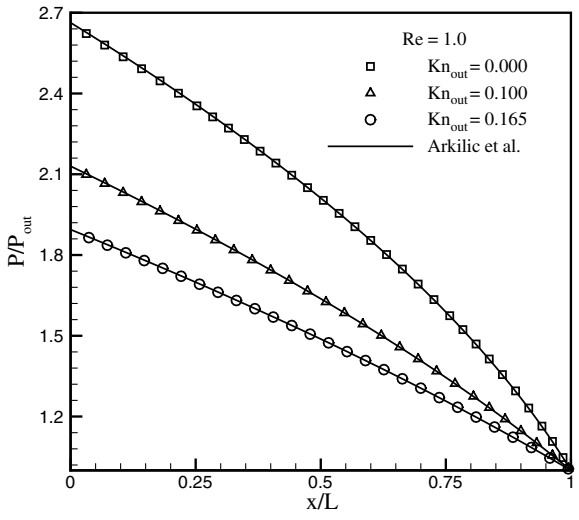


**Fig. 4 Comparison of numerical pressure distributions in a long microchannel with the analytical solution of Arkilic et al. [16].**

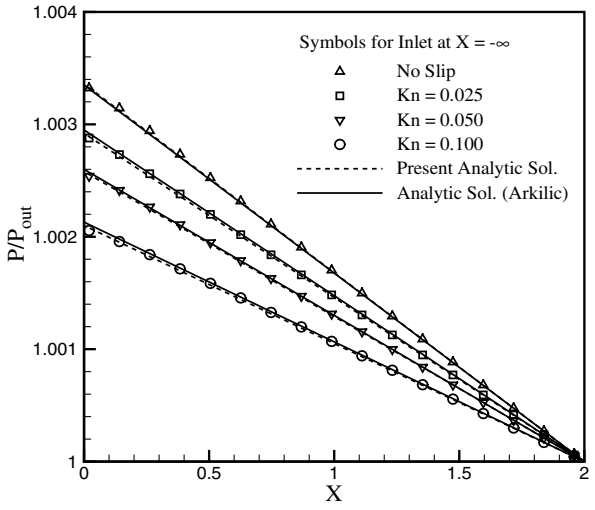


**Fig. 5 Comparison of pressure distributions in a short microchannel with the current analytical solution and the solution provided by Arkilic et al. [16].**

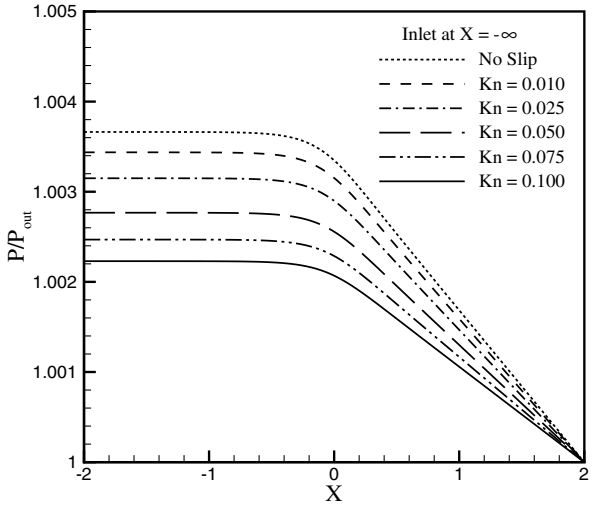


**a) Along the channel centerline**

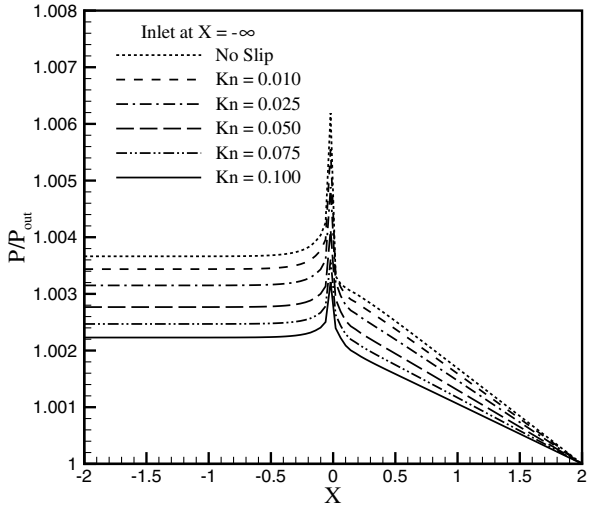


**b) Along the upper boundary of the solution domain**

**Fig. 6 Pressure distributions in a short microchannel for a few Knudsen numbers.**

region. This nonlinear behavior was similarly observed close to the inlet section of the microchannel in Fig. 5. As observed in these two plots, a higher Knudsen number results in a lower pressure drop in the microchannel. This is rather normal, because a lower Knudsen number causes a more pronounced no-slip condition at the wall. A reduction in the friction factor would normally cause less pressure drop along the channel. On the other hand, the rate of pressure drop near the inlet section in Fig. 6a is lower than that in Fig. 6b, whereas the pressure drops approach a constant rate in the rest of the channel in both figures. This behavior is due to the developing zone close to the inlet section and the singular point located at the beginning of the wall. They cause different pressure-drop behaviors close to the inlet region.

The distributions given in Fig. 6 can be broken into three parts, irrespective of the chosen Knudsen number. The first part is the region between the fictitious and actual inlet sections. As shown in Fig. 2, there is no reason to have a pressure drop far upstream of the actual inlet. The second part is the region close to the actual inlet section, which performs a nonlinear behavior. There is an abrupt disturbance close to the real inlet section, which is due to the fluid and solid wall interaction around the first node close to the inlet section. This point was elaborated in the Introduction. The jump can be attributed to the singularity generated at the beginning of the channel wall. In macroflow cases, the flow needs to be stagnated completely at this point, resulting in a strong jump in velocity magnitude at this point. Darbandi et al. [2,3] clearly explained why such disturbances

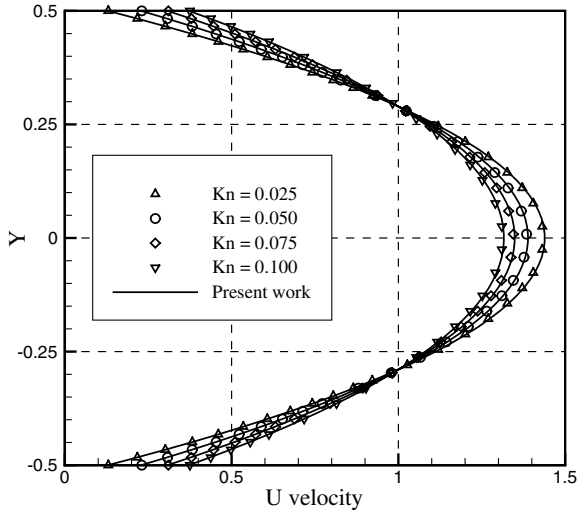


**Fig. 7 Comparison of numerical slip velocity profiles with the analytical solutions (symbols) given by Eq. (12) for a few Knudsen numbers.**

can occur in macrochannels. This singularity is similarly observed in microflow cases. However, the singularity would be less pronounced in microchannels, because of the Knudsen layer and slip behavior close to the solid wall. Eventually, the last part is the fully developed zone in the channel, in which the pressure drop becomes linear. The implement of inlet boundary conditions far upstream of the actual inlet section reduces the ambiguities in the developing zone of the microchannel and helps to achieve more pronounced results close to the inlet section of the microchannel.

After describing the pressure field in our short microchannel, we would like to study the details of the velocity field in the channel for a few Knudsen numbers, using either analytical solution or numerical predictions. Figure 7 shows the fully developed velocity profiles achieved at the outflow section for Knudsen numbers of 0.025, 0.05, 0.075, and 0.1. The current fully developed velocity profiles at the outflow section are compared with the analytical solutions given by Eq. (12). Symbols denote the analytical solutions and solid lines illustrate the numerical solution. There is excellent agreement between the numerical results and the analytical solutions, indicating that the channel is long enough to achieve a fully developed slip profile within the channel at the chosen Reynolds number. As shown in Fig. 7, a higher Knudsen number causes a higher slip at the solid wall and a lower peak at the centerline. The results are restricted to the slip flow regime, in which the chosen first-order slip boundary condition seems to work perfectly.

Because we place the inlet boundary conditions far upstream of the inlet section, it is necessary to ensure that this displacement has no adverse impact in the velocity profiles obtained in the fully developed region. In other words, it should be verified that nothing is lost during the implementation of symmetric boundary conditions upstream of the real inlet section (see Fig. 2). Figure 8 demonstrates the velocity profiles at the outlet of the microchannel, with the inlet boundary conditions implemented at two locations: $x/H = 0$ and $-2$. The latter location is referred as $-\infty$ in the figure, to emphasize that the fictitious section is sufficiently far from the real inlet section; hence, the free upstream conditions can be safely applied there. We employed our extended boundary conditions at the latter location and those of [18,20] at the former one. As shown in Fig. 8, there is no difference in the velocity profiles, despite switching from one location with one type of inlet boundary condition to another one with a second type of boundary condition. Therefore, we can state that the impact of inlet boundary condition on the fully developed slip velocity profile achieved at the outlet of the microchannel is irrelevant.

To study the details of velocity field solution, we derive the results in two ways. In other words, we study the solution domain by choosing two different computational domains and two different inlet boundary conditions (see Fig. 8). However, to magnify the uncertainties in the velocity field solution within the entrance region,

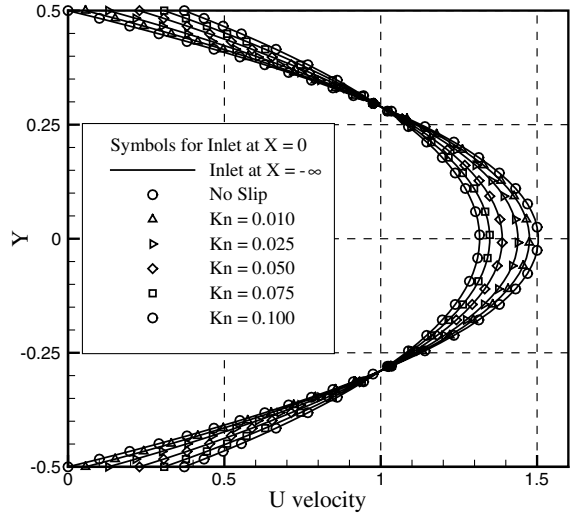


**Fig. 8 Comparison of predicted slip velocity profiles for two inlet boundary conditions at two locations.**

we follow the approach taken in Fig. 8 and apply either a uniform inlet boundary condition at the fictitious inlet section or a fully developed no-slip velocity profile at the actual inlet section.

Figure 9 presents the centerline velocity magnitude in the computational domain using the two approaches. As can be seen, the

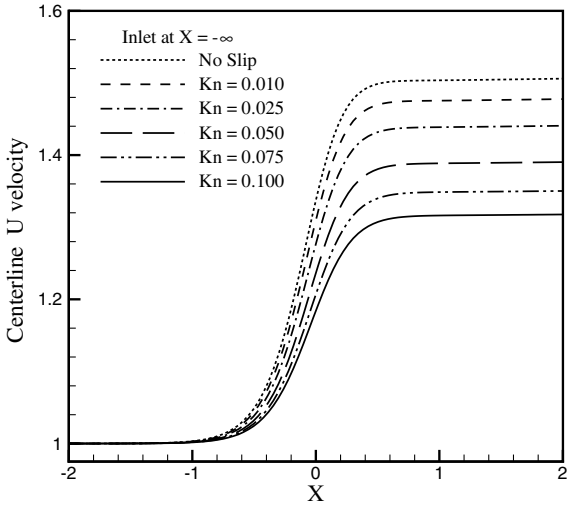


**a) Using the current fictitious inlet**

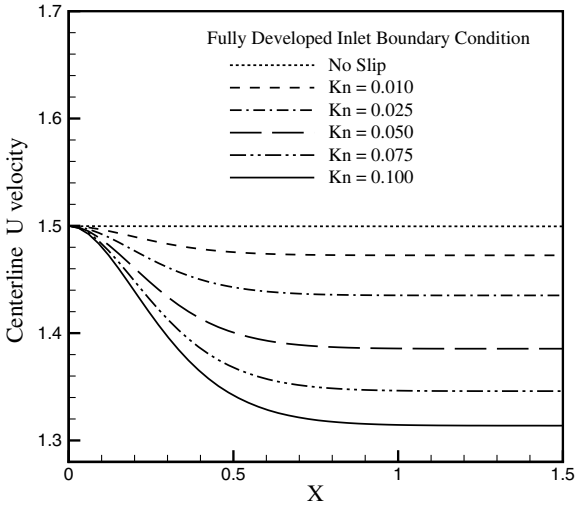


**b) Using the actual inlet**

**Fig. 9 Centerline velocity distribution in the computational domain.**

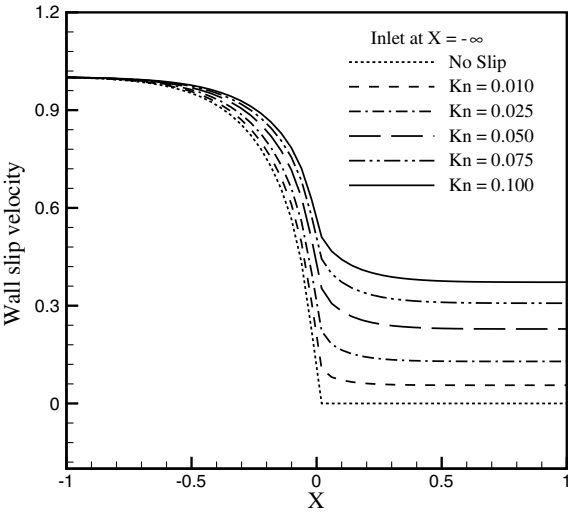


**a) Using the current fictitious inlet**

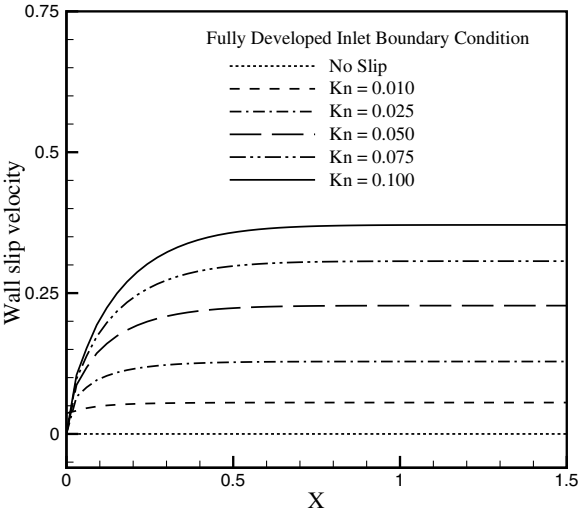


**b) Using the actual inlet**

**Fig. 10 Wall slip velocity magnitude in the computational domain.**

solutions in the entrance region vary with the two approaches; however, the achieved solutions in the fully developed region are the same. The entrance-region length in short microchannels is on the order of the channel length, which causes uncertainty in the numerical solution of short channels. Comparing Fig. 9a with Fig. 9b, it is rational to be in favor of the approach taken in Fig. 9a, because it does not enforce an unrealistic boundary condition at the actual inlet section of the microchannel. Contrary to Fig. 9b, Fig. 9a permits the velocity profiles to develop suitably and to reach a more realistic solution at the actual inlet section. Careful inspection of the two figures indicates that the entrance-region lengths are different, from taking different approaches.

Similar to Fig. 9, Fig. 10 presents the velocity magnitude along the upper boundary of the computational domain. Assuming a no-slip flow condition, there is no difference between the corresponding results in Figs. 10a and 10b. However, the difference becomes dominant as the Knudsen number increases and the slip flow regime becomes serious. The plots in Fig. 10 support the outcomes achieved by inspecting the two plots in Fig. 9. Generally speaking, the use of different boundary conditions at different inlet locations causes different slip flow magnitudes on the wall, different wall shear stress effects, and thus different pressure drop calculations in the entrance region. Similar to our past study of macrochannels [2], the friction factor calculation is influenced by the choice of boundary conditions and the locations in which they are applied. Of course, the current study suggests a sounder location, to achieve a more accurate solution in the entrance region of the channel.

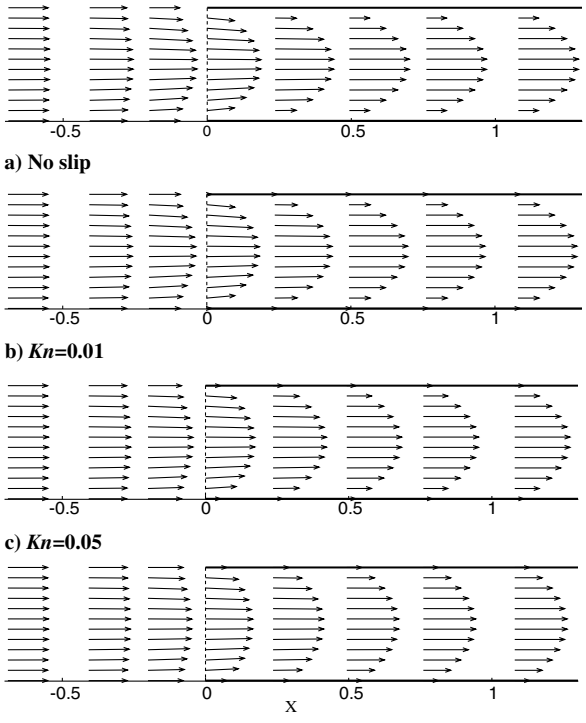


**Fig. 11 Selected velocity vector plots in the solution domain.**

Figure 11 illustrates the velocity vector plots in eight locations in a part of the extended solution domain using $Kn = 0.0, 0.01, 0.05$, and 0.1. The chosen longitudinal locations are $x/H = -0.69$, $-0.41$, $-0.20$, 0.0, 0.24, 0.49, 0.76, and 1.08, of which three are located upstream of the inlet section and one is at the real inlet section. The inlet boundary conditions are applied at fictitious locations in all cases. The velocity profiles can be compared with each other from different perspectives. Figures 11a and 11b indicate no slip and negligible slip on the wall, respectively. However, Figs. 11c and 11d show that the slip behavior becomes important at high Knudsen numbers. Generally, Fig. 11 demonstrates that the uniform inlet velocity at the fictitious location is gradually deformed in the upstream region of the real inlet section and reaches a limiting suitable profile at this section. The profile at the real inlet section does not have a unique shape as the Knudsen number changes. Indeed, the shape depends on both the Reynolds and Knudsen numbers as well as the type of boundary conditions applied on the upstream horizontal boundaries. Figures 7 and 8 and the velocity vector plots in Fig. 11 for $X/H > 1.0$ indicate that the change in inlet boundary conditions affects the solution in the entrance region, but not that in the fully developed region. In other words, the use of a uniform flat velocity profile at the actual inlet section can result in incorrect developing-zone solutions. Despite this fact, almost all of the references in the Introduction apply a uniform inlet velocity profile at the real inlet of the channel. As already mentioned, it is because the entrance regions occupy small parts of their long microchannels.

To quantify the impact of chosen boundary conditions on the entrance-region solution, Table 1 presents the entrance length for various Knudsen numbers and two types of inlet boundary conditions. The entrance length is defined as a longitudinal distance from the real inlet section to the point at which the centerline velocity reaches 99% of its asymptotic value. As indicated in the table, there is no developing zone for the case with $Kn = 0.0$ if a fully developed velocity profile is employed at the real inlet section. Otherwise, there is always a developing zone close to the channel inlet, in which the length depends on the magnitude of the Knudsen number and the way that the inlet boundary conditions are applied at its inlet. The table also indicates that the entrance length is less sensitive to the Knudsen number in high Knudsen number magnitudes if the inlet boundary conditions are applied at the fictitious section. However, if the fully developed no-slip velocity profile is applied at the real inlet section, the entrance length is affected by the change of the Knudsen number in all Knudsen number regimes.

**Table 1 Comparison of entrance lengths for two types of inlet boundary conditions applied at two locations**

| $Kn$ | Type of boundary condition | |
|---|---|---|
| | Fully developed no-slip velocity at $x/H = 0$ | Uniform velocity at $x/H = -\infty$ |
| 0.000 | 0.000 | 0.648 |
| 0.010 | 0.770 | 0.729 |
| 0.025 | 0.892 | 0.810 |
| 0.050 | 1.014 | 0.830 |
| 0.075 | 1.136 | 0.850 |
| 0.100 | 1.216 | 0.871 |

Darbandi et al. [35] used the current numerical approach and described the history of the slip velocity residuals during the iterations and compared them with each other from different perspectives. They indicated that a lower under-relaxation parameter would be required to implement the slip conditions. In other words, the slip velocity residuals need more iterations to decrease to a specified criterion at higher Knudsen numbers. Evidently, the choice of an improper under-relaxation parameter can increase the number of iterations dramatically. Moreover, there would be always an optimum magnitude for the under-relaxation parameter to perform the best possible convergence rate.

## VII. Conclusions

The uniform inlet boundary conditions used regularly in numerical treatment of microchannel flows cannot be confidently applied in microchannels in which the lengths are comparable with the lengths of their hydrodynamic developing zone in the channel. The essence of difficulty stems from the interaction of the wall slip flow condition and the flat inlet velocity condition. This singularity at the inlet of the channel has prompted previous researchers to choose fully developed no-slip velocity profiles at the inlet of their microchannels, which is not very realistic and can effectively deteriorate the accuracy of the calculation in the entrance region of the microchannel. To overcome this difficulty, we applied physical boundary conditions far upstream of the real channel inlet. Using this extended channel, the short microchannels were tested for a wide range of Knudsen numbers, from the no-slip to the slip flow regime and the early transition regime. It was shown that the current solutions have excellent agreement with other available reference solutions at the investigated Knudsen numbers. Additionally, the use of new consistent slip velocity boundary conditions results in a solution that is less sensitive to its Knudsen number, providing that the Knudsen number is sufficiently large. The current investigation showed that the new strategy would result in more accurate solutions in the region close to the inlet section of microchannels.

## Acknowledgment

The present work was supported by the research center of the Sharif University of Technology under grant SUTRC- 84-4105. The support is gratefully acknowledged.

## References

[1] Kakac, S., Shah, R. K., and Bergles, A. E., *Low Reynolds Number Flow Heat Exchangers*, Hemisphere, New York, 1983.

[2] Darbandi, M., and Hosseinizadeh, S. F., "Remarks on Numerical Prediction of Wall Shear Stress in Entry Flow Problems," *Communications in Numerical Methods in Engineering*, Vol. 20, No. 6, 2004, pp. 619–625.

[3] Darbandi, M., and Schneider, G. E., "Numerical Study of the Flow Behavior in the Uniform Velocity Entry Flow Problem," *Numerical Heat Transfer, Part A, Applications*, Vol. 34, No. 5, 1998, pp. 479–494.

[4] Wang, Y. L., and Longwell, P. A., "Laminar Flow in the Inlet Section of Parallel Plates," *AIChE Journal*, Vol. 10, No. 3, 1964, pp. 323–329.

[5] Mcdonald, J. W., Denny, V. E., and Mills, A. F., "Numerical Solutions of the Navier–Stokes Equations in Inlet Region," *Journal of Applied Mechanics*, Vol. 39, No. 4, 1972, pp. 873–878.
[6] Morihara, H., and Cheng, R. T., "Numerical Solution of Viscous Flow in the Entrance Region of Parallel Plates," *Journal of Computational Physics*, Vol. 11, No. 4, 1973, pp. 550–572.
[7] Chen, R. Y., "Flow in the Entrance Region at Low Reynolds Numbers," *Journal of Fluids Engineering*, Vol. 95, Mar. 1973, pp. 153–158.
[8] Chilukuri, R., and Pletcher, R. H., "Numerical Solutions to the Partially Parabolized Navier–Stokes Equations for Developing Flow in a Channel," *Numerical Heat Transfer*, Vol. 3, June 1980, pp. 169–188.
[9] Abdulnour, B. S., and Potter, M. C. "A Stable, Iterative Finite-Difference Procedure for the Navier–Stokes," *Proceedings of the ASME Fluids Engineering Division*, Vol. 93, American Society of Mechanical Engineers, New York, 1990, pp. 15–19.
[10] Karniadakis, G. E., Beskok, A., and Aluru, N., *Microflows and Nanoflows: Fundamentals and Simulation*, Springer–Verlag, New York, 2005.
[11] Pfahler, J., Harley, J., Bau, H., and Zemel, J. N., "Gas and Liquid Flow in Small Channels," *Micromechanical Sensors, Actuators, and Systems*, Vol. 32, American Society of Mechanical Engineers, Dynamic Systems and Control Div., New York, 1991, pp. 49–60.
[12] Choi, S. B., Barron, R. F., and Warrington, R. O., "Fluid Flow and Heat Transfer in Micro Tubes," *Micromechanical Sensors, Actuators, and Systems*, Vol. 32, American Society of Mechanical Engineers, Dynamic Systems & Control Div., New York, 1991, pp. 123–134.
[13] Pong, K. C., Ho, C., Liu, J., and Tai, Y., "Non-Linear Pressure Distribution in Uniform Microchannels," *Application of Microfabrication to Fluid Mechanics*, Vol. 197, American Society of Mechanical Engineers, Fluids Engineering Div., New York, 1994, pp. 51–56.
[14] Beskok, A., and Karniadakis, G. E., "Simulation of Heat and Momentum Transfer in Complex Microgeometries," *Journal of Thermophysics and Heat Transfer*, Vol. 8, No. 4, 1994, pp. 647–655.
[15] Shih, J. C., Ho, C. M., Liu, J., and Tai, Y. C., "Monoatomic and Polyatomic Gas Flow Through Uniform Microchannels," *Application of Microfabrication to Fluid Mechanics*, Vol. 59, American Society of Mechanical Engineers, Dynamic Systems & Control Div., New York, 1996, pp. 197–203.
[16] Arkilic, E. B., Schmidt, M. A., and Breuer, K. S., "Gaseous Slip Flow in Long Microchannels," *Journal of Microelectromechanical Systems*, Vol. 6, No. 2, 1997, pp. 167–178.
[17] Kavehpour, H. P., and Faghri, M., "Effects of Compressibility and Rarefaction on Gaseous Flows in Microchannels," *Numerical Heat Transfer, Part A, Applications*, Vol. 32, Nov. 1997, pp. 677–696.
[18] Guo, Z. Y., and Wu, X. B., "Further Study on Compressibility Effects on the Gas Flow and Heat Transfer in a Microtube," *Microscale Thermophysical Engineering*, Vol. 2, No. 2, 1998, pp. 111–120.
[19] Beskok, A., and Karniadakis, G. E., "A Model for Flows in Channels, Pipes and Ducts at Micro and Nano Scales," *Microscale Thermophysical Engineering*, Vol. 3, No. 1, 1999, pp. 43–77.
[20] Barber, A. B., and Emerson, D. R., "A Numerical Study of Low Reynolds Number Slip Flow in the Hydrodynamic Development Region of Circular and Parallel Plate Ducts," Council for the Central Laboratory of the Research Councils (CCLRC), Rept. DL-TR-00-002, Daresbury Lab., Cheshire, England, U.K., 2000.
[21] Ahmed, I., and Beskok, A., "Rarefaction, Compressibility, and Viscous Heating in Gas Microfilters," *Journal of Thermophysics and Heat Transfer*, Vol. 16, No. 2, 2002, pp. 161–170.
[22] Choi, H., Lee, D., and Maeng, J. S., "Computation of Slip Flow in Microchannels Using Langmuir Slip Condition," *Numerical Heat Transfer, Part A, Applications*, Vol. 44, No. 1, 2003, pp. 59–71.
[23] Asako, Y., and Toriyama, H., "Heat Transfer Characteristics of Gaseous Flows in Microchannels," *Microscale Thermophysical Engineering*, Vol. 9, No. 1, 2005, pp. 15–31.
[24] Raju, R., and Roy, S., "Modeling Single Component Fluid Transport Through Micro Channel and Free Molecule Micro-Resistojet," 42nd Aerospace Sciences Meeting and Exhibit, Reno, NV, AIAA Paper 2004-1342, 2004.
[25] Raju, R., and Roy, S., "Hydrodynamic Study of High-Speed Flow and Heat Transfer Through a Microchannel," *Journal of Thermophysics and Heat Transfer*, Vol. 19, No. 1, 2005, pp. 106–113.
[26] Darbandi, M., and Schneider, G. E., "Performance of an Analogy-Based All-Speed Procedure Without Any Explicit Damping," *Computational Mechanics*, Vol. 26, No. 5, 2000, pp. 459–469.
[27] Darbandi, M., Rouhi, E., and Mokarizadeh, V., "Conceptual Linearization of Euler Governing Equations to Solve High Speed Compressible Flow Using a Pressure-Based Method," *Numerical Methods for Partial Differential Equations* (to be published).
[28] Renksizbulut, M., Niazmand, H., and Tercan, G., "Slip-Flow and Heat Transfer in Rectangular Microchannels with Constant Wall Temperature," *International Journal of Thermal Sciences*, Vol. 45, No. 9, 2006, pp. 870–881.
[29] Oran, E. S., Oh, C. K., and Cybyk, B. Z., "Direct Simulation Monte Carlo: Recent Advances and Applications," *Annual Review of Fluid Mechanics*, Vol. 30, Jan. 1998, pp. 403–441.
[30] Shen, C., Fan, J., and Xie, C., "Statistical Simulation of Rarefied Gas Flows in Micro-Channels," *Journal of Computational Physics*, Vol. 189, 2003, pp. 512–526.
[31] Shu, C., Niu, D., and Chew, Y. T., "A Lattice Boltzmann Kinetic Model for Microflow and Heat Transfer," *Journal of statistical Physics*, Vol. 121, Oct. 2005, pp. 239–255.
[32] Niu, X. D., Shu, C., and Chew, Y. T., "A Thermal Lattice Boltzmann Model with Diffusive Scattering Boundary Condition for Micro Thermal Flows," *Computers and Fluids*, Vol. 36, No. 2, 2007, pp. 273–281.
[33] Le, M., and Hassan, I., "Simulation of Heat Transfer in High Speed Microflows," *Applied Thermal Engineering*, Vol. 26, No. 16, 2006, pp. 2035–2044.
[34] Gampert, B., "Inlet Flow with Slip," in *Rarefied Gas Dynamics*, edited by J. Potter, AIAA, New York, 1977.
[35] Darbandi, M., Vakilipour, S., and Schneider, G. E., "Development of a Consistent Slip-Boundary Condition at the Inlet of Microchannels," 44th AIAA Aerospace Sciences Meeting and Exhibit, Reno, NV, AIAA Paper 2006-0591, 2006.
[36] Fichman, M., and Hetsroni, G., "Viscousity and Slip Velocity in Gas Flow in Microchannels," *Physics of Fluids*, Vol. 17, No. 1, 2005, pp. 1–5.
[37] Harley, J., Huang, Y., Bau, H., and Zemel, J. N., "Gas Flow in Micro-Channels," *Journal of Fluid Mechanics*, Vol. 284, Feb. 1995, pp. 257–274.
[38] Darbandi, M., and Hosseinizadeh, S. F., "General Pressure-Correction Strategy to Include Density Variation in Incompressible Algorithms," *Journal of Thermophysics and Heat Transfer*, Vol. 17, No. 3, 2003, pp. 372–380.
[39] Jahn, R., *Physics of Electric Propulsion*, McGraw–Hill, New York, 1968.
[40] Wong, J., Ketsdever, A., and Reed, H., "Numerical Modeling of the Free Molecule Micro-Resistojet Prototype and Next Generation Designs Evaluation," 36th Thermophysics Conference, Orlando, FL, AIAA Paper 2003-3581, 2003.
[41] Mott, D. R., Oran, E. S., and Kaplan, C. R., "Microfilter Simulations and Scaling Laws," *Journal of Thermophysics and Heat Transfer*, Vol. 15, No. 4, 2001, pp. 473–477.
[42] Lin, Y. L., Chyu, M. K., Shih, T. I. P., Willis, B. P., and Hwang, D. P., "Skin-Friction Reduction Through Micro Blowing," 36th Aerospace Sciences Meeting and Exhibit, Reno, NV, AIAA Paper 1998-0359, 1998.
[43] Basset, A. B., *A Treatise on Hydrodynamics*, Cambridge Univ. Press, Cambridge, England, U.K., 1888.
[44] Schaaf, S. A., and Chambre, P. L., *Flow of Rarefied Gases*, Princeton Univ. Press, Princeton, NJ, 1961.
[45] Darbandi, M., and Vakilipour, S., "Developing Implicit Pressure-Weighted Upwinding Scheme to Calculate Steady and Unsteady Flows on Unstructured Grids," *International Journal for Numerical Methods in Fluids* (to be published).
[46] Darbandi, M., and Schneider, G. E., "Momentum Variable Procedure for Solving Compressible and Incompressible Flows," *AIAA Journal*, Vol. 35, No. 12, 1997, pp. 1801–1805.
[47] Rhie, C. M., and Chow, W. L., "Numerical Study of the Turbulent Flow Past an Airfoil with Trailing Edge Separation," *AIAA Journal*, Vol. 21, No. 11, 1983, pp. 1525–1532.
[48] Darbandi, M., and Bostandoost, S. M., "A New Formulation Toward Unifying the Velocity Role in Collocated Variable Arrangement," *Numerical Heat Transfer, Part B, Fundamentals*, Vol. 47, No. 4, 2005, pp. 361–382.
[49] Darbandi, M., and Schneider, G. E., "Analogy-Based Method for Solving Compressible and Incompressible Flows," *Journal of Thermophysics and Heat Transfer*, Vol. 12, No. 2, 1998, pp. 239–247.
[50] Darbandi, M., Schneider, G. E., and Vakili, S., "Using Different Preconditioned Krylov Subspace Methods to Solve Coupled Fluid Flow Equations," *Computational Fluid Dynamics Journal*, Vol. 15, No. 1, 2006, pp. 35–43.
[51] Darbandi, M., and Vakilipour, S., "Using Fully Implicit Conservative Statements to Close Open Boundaries Passing Through Recirculations," *International Journal for Numerical Methods in Fluids*, Vol. 53, No. 3, 2007, pp. 371–389.

[52] Alishahi, M. M., and Darbandi, M., "Multiple-Zone Potential Solution Around Wing-Body Configurations," *Journal of Aerospace Engineering*, Vol. 6, No. 4, 1993, pp. 329–346.

[53] Burke, J. P., and Berman, N. S., "Entrance Flow Development in Circular Tubes at Small Axial Distances," American Society of Mechanical Engineers Paper 69-WA/FE-13, 1969.

[54] Jang, J., and Wereley, S. T., "Pressure Distributions of Gaseous Slip Flow in Straight and Uniform Rectangular Microchannels," *Microfluidics and Nanofluidics*, Vol. 1, No. 1, 2004, pp. 41–51.